HHS Public Access

Author manuscript

Science. Author manuscript; available in PMC 2022 August 07.

Published in final edited form as:

Science. 2022 March 18; 375(6586): 1287–1291. doi:10.1126/science.abm3282.

Recovery of particulate methane monooxygenase structure and activity in a lipid bilayer

Christopher W. Koo[1], **Frank J. Tucci**[1], **Yuan He**[1], **Amy C. Rosenzweig**[1,2,*]

[1]Department of Molecular Biosciences, Northwestern University, Evanston, IL 60208, USA

[2]Department of Chemistry, Northwestern University, Evanston, IL 60208, USA.

Abstract

Bacterial methane oxidation using the enzyme particulate methane monooxygenase (pMMO) contributes to the removal of environmental methane, a potent greenhouse gas. Crystal structures determined using inactive, detergent-solubilized pMMO lack several conserved regions neighboring the proposed active site. We show that reconstituting pMMO in nanodiscs with lipids extracted from the native organism restores methane oxidation activity. Multiple nanodiscembedded pMMO structures determined by cryo–electron microscopy to 2.14- to 2.46-angstrom resolution reveal the structure of pMMO in a lipid environment. The resulting model includes stabilizing lipids, regions of the PmoA and PmoC subunits not observed in prior structures, and a previously undetected copper-binding site in the PmoC subunit with an adjacent hydrophobic cavity. These structures provide a revised framework for understanding and engineering pMMO function.

Methane, a potent greenhouse gas, is a major contributor to the current climate crisis (1, 2). Methane-oxidizing (methanotrophic) bacteria not only consume ~30 million metric tons of atmospheric methane per year (3) but also have the biotechnological potential to convert this cheap and abundant feedstock to fuels and value-added chemicals (4). Although methanotrophs have been engineered to produce a range of products, low yields and conversion efficiencies have precluded economic viability (5). For methane bioconversion to be transformative, the initial step—oxidation of methane to methanol—must be optimized, which requires molecular-level understanding of the main enzyme responsible, particulate methane monooxygenase (pMMO) (6, 7).

pMMO is a membrane-bound, copper-dependent enzyme comprising three subunits, PmoA (β), PmoB (α), and PmoC (γ), arranged as a trimer of αβγ protomers. The crystal structures of detergent-solubilized pMMO from multiple methanotrophic species (8–12) have revealed the presence of three copper-binding sites. The ligands to two monocopper sites located in PmoB, the bis-His site and the Cu_B site, are not conserved, with the bis-His site

*Corresponding author. amyr@northwestern.edu.

Author contributions: Conceptualization: C.W.K., F.J.T., and A.C.R. Methodology: C.W.K., F.J.T., Y.H., and A.C.R. Investigation: C.W.K. and F.J.T. Visualization: C.W.K. and F.J.T. Funding acquisition: A.C.R. Project administration: A.C.R. Supervision: A.C.R. and Y.H. Writing – original draft: C.W.K., F.J.T., and A.C.R. Writing – review and editing: C.W.K., F.J.T., Y.H., and A.C.R.

Competing interests: The authors declare that they have no competing interests.

only present in pMMOs of Gammaproteobacteria and the Cu_B site missing in pMMOs of Verrucomicrobia (13). By contrast, one aspartic acid and two histidine ligands to the third site, Cu_C, located in PmoC, are strictly conserved. This observation, along with the saturated coordination geometry of the Cu_B site and the correlation of increased methane oxidation activity with copper occupancy of PmoC (14), suggests that the copper active site is located in PmoC.

However, it remains unclear whether the crystallographic Cu_C site is an appropriate active site model owing to several major caveats with the crystal structures. First, pMMO activity decreases upon solubilization in detergent (11, 15), and purified samples exhibit zero methane oxidation activity (table S1), which means that the structures do not represent the active enzyme. Second, ~25 residues within PmoC are not observed in the electron density maps for any pMMO crystal structure. These residues, which correspond to the most highly conserved part of the PmoC sequence, are predicted to reside adjacent to the Cu_C site facing the interior of the pMMO trimer (6). The ambiguity in this region has precluded the identification of any potential cavities for methane and oxygen binding. It is likely that both of these limitations—the loss of activity and the disorder in PmoC—are attributable to the removal of pMMO from its native membrane environment. Disruption of the lipid bilayer followed by detergent solubilization and multiple purification steps may cause conformational changes and the separation of bound metal and/or lipid cofactors (16, 17).

We recently demonstrated that reconstitution of detergent-solubilized pMMO into synthetic lipid bicelles (11) and nanodiscs (14) restores methane oxidation activity (table S1). To prepare enzymatically active samples for structure determination by cryo–electron microscopy (cryo-EM), *Methylococcus capsulatus* (Bath) pMMO was solubilized in *n*-dodecyl-β-D-maltoside (DDM) and embedded into nanodiscs using the membrane scaffold protein MSP1E3D1 and the commonly used lipids 1,2-dimyristoyl-sn-glycero-3-phosphocholine(DMPC) and 1-palmitoyl-2-oleoylphosphatidylcholine (POPC) (18). To more closely mimic the cellular environment of pMMO, native lipids were extracted from *M. capsulatus* (Bath) (19, 20) and used for nanodisc reconstitution. Nanodisc formation and pMMO incorporation were confirmed by negative-stain EM and cryo-EM (fig. S1).

As observed previously for *Methylocystis* species (sp.) strain (str.) Rockwell pMMO (14), the addition of copper during nanodisc reconstitution was necessaryto recover methane oxidation activity. Nanodiscs formed with 3 molar equivalents of $CuSO_4$ and the native lipids exhibited the most activity, followed by POPC and DMPC nanodiscs (Fig. 1A and fig. S2). The copper content also increased slightly in the native and POPC nanodiscs (fig. S3). The looser packing afforded by the unsaturated bond in the acyl tails of POPC (11) and the native lipids (vide infra) may facilitate the loading of individual copper sites as well as access of the reductant used in the activity assays, duroquinol, to the active site. The observed turnover frequency of 0.012 s^{-1} represents a substantial improvement over the zero activity Cymal-5 samples used for previous structural studies and is comparable to *M. capsulatus* (Bath) membrane-bound pMMO activity measured with duroquinol (0.025 to 0.042 s^{-1}) (table S1). Notably, duroquinol is a synthetic analog of endogenous quinols (21) and is not the physiological reductant as has been claimed

recently (22). In vivo electron delivery has been proposed to occur through ubiquinol reduced by a type 2 NADH:oxidoreductase and/or by coupling to methanol oxidation by methanol dehydrogenase (MDH) (6). The absence of these potential redox partners may be what precludes attaining whole-cell activity using isolated pMMO. Moreover, negative-stain images of *M. capsulatus* (Bath) membranes show dense packing of pMMO trimers (fig. S4), an environment that may contribute to increased activity in the membrane and that cannot be recapitulated in a single particle study.

Six cryo-EM maps of nanodisc-embedded pMMO from three different methanotrophs were obtained to 2.14- to 2.46-Å resolution (figs. S5 and S6 and table S2), providing the first structures of pMMO in a lipid environment. The highest-resolution map is that of enzymatically active *M. capsulatus* (Bath) pMMO in native lipid nanodiscs, resolved to 2.14 Å (MC01; table S2 and Fig. 1B), which is considerably higher resolution than that of the *M. capsulatus* (Bath) (2.8Å) (8), the *Methylocystis* sp. str. Rockwell (2.6 Å) (10), and the *Methylotuvimicrobium alcaliphilum* combination (comb.) nova (nov.) 20Z (2.7 Å) (11) pMMO crystal structures. The overall architecture agrees with the crystal structures, consisting of a trimer of αβγ protomers within the nanodisc belt (Fig.1B). Densities corresponding to solvent molecules and phospholipids (Fig. 1C and fig. S7) are clearly defined at this resolution.

The two periplasmic cupredoxin domains of PmoB extend out of the nanodisc (Fig. 1B) and exhibit the same folds as observed crystallographically, with two copper sites readily apparent in each cryo-EM map. The Cu_B site is coordinated by His^{33}, His^{137}, His^{139}, and the N terminus of PmoB in a square planar geometry (Fig. 2). Additionally, two water molecules, located 3.6 to 3.7 Å from the copper ion, stabilize the site through hydrogen-bonding interactions. Although axial water ligands were identified in crystallographic and spectroscopic studies of Cu_B (10, 23–25), the observed water molecules are too distant for coordination. As in the crystal structures, the density for His^{33} and the N terminus is less clear, which suggests that it is somewhat flexible. The Cu_B site is unequivocally mononuclear (fig. S8), in contrast to a recent cryo-EM structure of *M. capsulatus* (Bath) pMMO in DDM (26) but consistent with recent spectroscopic (23, 24, 27) and computational (25) studies. The corresponding Cu_B sites in the cryo-EM structures of pMMO from *Methylocystis* sp. str. Rockwell and *M. alcaliphilum* comb. nov. 20Z exhibit the same mononuclear structures (RW01 and 20Z01; table S2 and fig. S8).

The bis-His site, coordinated by residues His^{48} and His^{72} (Fig. 2), is also present, consistent with the *M.capsulatus* (Bath) pMMO crystal structure (8). This site is occupied in the *M. alcaliphilum* comb. nov. 20Z pMMO cryo-EM map (fig. S8), despite being unoccupied in the crystal structure (11). The ligand corresponding to His^{48} is replaced with asparagine in *Methylocystis* sp. str. Rockwell pMMO, and the bis-His site is unoccupied (fig. S8). Whereas a recent cryo-EM study of *M. capsulatus* (Bath) pMMO in DDM suggested the presence of three additional copper ions in PmoB (26), no density at these specific locations is apparent in any of the maps of active pMMO in nanodiscs (fig. S9). There is no support in any of the structures for prior claims that a so-called Cu(I) sponge in PmoB mediates electron transfer (26, 28).

In the transmembrane region, lipids coat the exterior of pMMO (Fig. 1C), with a total of 36 lipids modeled into the map as phosphatidylcholines along with 18 acyl chains, of which the head groups are not visible (fig. S7).A bilayer is observed in the interior of the pMMO trimer, showing that what appears to be a pore in the crystal structures is filled by phospholipids when embedded in a membrane-like environment (Fig. 1C). The longest acyl chain could be resolved to 12 carbons, with the density becoming less clear as the tails extend toward the middle of the bilayer. To investigate the possible identities of these native phospholipids, both *M. capsulatus* (Bath) whole cells and the native lipid pMMO-nanodisc complex were subjected to lipidomics analysis by liquid chromatography–tandem mass spectrometry (LCMS/MS). A mixture of phosphatidylethanolamine (PE), phosphatidylcholine (PC), phosphatidylglycerol (PG), and cardiolipin (CL) was identified (fig. S10). For comparison, the structure of *M. capsulatus* (Bath) pMMO in a POPC nanodisc was determined to 2.26-Å resolution (MC02; table S2). The lipid densities appear very similar between the two maps, which suggests that most of the observed lipids are PC lipids (fig. S11), although other native lipids may remain associated with pMMO through the nanodisc reconstitution process. One exterior lipid density exhibits an unusual shape, which suggests that it may have a different identity, such as a native quinone that remains bound during purification and nanodisc reconstitution (fig. S11). This density occupies the position filled by an unidentified helix in the *Methylocystis* sp. str. Rockwell pMMO crystal structure (10) and in the cryo-EM structure (RW01).

Several regions of *M.capsulatus* (Bath) pMMO that were not observed in the crystal structures are ordered in the cryo-EM maps. PmoA residues 192 to 212 are stabilized by phospholipids on the interior and exterior of the enzyme (Fig. 3A). This part of PmoA extends into PmoC, with PmoA residue Arg^{206} forming a hydrogen bond with PmoC residue Glu^{238} (Fig. 3B), a strictly conserved residue not observed in the crystal structures (Fig. 3, C and D). There is no evidence for a tricopper D site proposed to be depleted from the inactive pMMO (29). Although two of the three copper ions in this putative site were recently modeled in the cryo-EM structure of *M. capsulatus* (Bath) pMMO in DDM (26), our high-resolution maps instead show Glu^{154} and a water molecule in the region (fig. S12).This water molecule forms hydrogen bonds with putative tricopper ligands Glu^{100} from PmoA and Glu^{154} from PmoC, which in turn is hydrogen bonded to Asn^{103} from PmoA, also claimed to be a ligand (26). The other hypothetical ligands, His^{38} and Met^{42}, do not interact with any additional densities that could be attributed to copper ions (fig. S12). Moreover, a suggested hydrophobic pocket for substrate binding involving Trp^{48}, Phe^{50}, Trp^{51}, and Trp^{54} (30) is occupied by Asp^{47} from PmoA.

The highly conserved region of PmoC (Fig. 3D) that was unmodeled in the crystal structures (Fig. 3C and fig. S13) and the recent cryo-EM structure of pMMO in DDM (26) is observed in all the cryo-EM maps (figs. S13 and S14). This region corresponds to residues 225 to 253 in *M. capsulatus* (Bath) pMMO. Hydrophobic residues from this sequence interact with phospholipid tails in the trimer interior, including close interactions between phospholipids and previously unmodeled residues (fig. S14). These interactions stabilize a four-helix bundle comprising residues 123 to 163 (α1), 170 to 199 (α2), 220 to 233 (α3), and 244 to 270 (α4) (Fig. 3A). The Cu_C ligands, Asp^{156}, His^{160}, and His^{173}, derive from helices α1 and α2. This structure is observed in each of the *M. capsulatus* (Bath) pMMO maps, including

the POPC nanodisc (MC02; table S2), which suggests that the stabilizing effect is imparted by the bilayer rather than a particular native lipid. The nanodisc and lipid environment may restore activity to pMMO (Fig. 1A) by stabilizing catalytically important features of this highly conserved region.

The environment of the crystallographically modeled Cu_C site is drastically altered in the cryo-EM structure. Newly observed helices α3 and α4 house three strictly conserved residues, Asn^{227}, His^{231}, and His^{245}, which extend toward the crystallographic Cu_C ligands Asp^{156}, His^{160}, and His^{173} (Fig. 3B). Residue Arg^{165}, which was hydrogen-bonded to Asp^{168} in the crystal structure (Fig. 3C), is now positioned near the Cu_C site via a hydrogen-bonding network to Glu^{238} and PmoA Arg^{206} (Fig. 3B and Fig. 4A). Arginine residues in hydrophobic environments play a variety of functional roles in enzymes, including regulating redox potentials and substrate binding (31, 32). Unexpectedly, Asn^{227}, His^{231}, and His^{245} are connected to a strong density that distinctly resembles a metal ion (Fig. 4B). This metal ion is ligated by the side-chain e nitrogens of the two histidine residues (Cu-N; 2.0 Å) and the side chain of Asn^{227} (2.35 Å) in a trigonal planar geometry (Fig. 4B). The metal ion density is more persistent than the surrounding protein density at higher thresholds and is present in the cryo-EM maps of three independent samples of *M. capsulatus* (Bath) pMMO in both native (table S2; MC01 and MC04) and POPC (table S2; MC02) nanodiscs (Fig. 4B and fig. S15). Given that copper restores activity to metal-depleted membranes (10) and to nanodisc samples (14), it is likely that the density corresponds to a previously unknown copper site, denoted here as Cu_D [not to be confused with the proposed D site in PmoA (26)]. The Glu^{228} carboxylate group is within hydrogen-bonding distance of the Asn^{227} side chain, consistent with hydrogen bonding via its side-chain amide group and coordination of copper by its side-chain oxygen atom (fig. S16). Copper coordination by the side-chain oxygen of asparagine or glutamine is unusual but not unprecedented (33–36). Recent X-band electron paramagnetic resonance (EPR) and electron nuclear double resonance (ENDOR) spectroscopic studies of *M. capsulatus* (Bath) pMMO in POPC nanodiscs indicate the presence of two histidine ligands to the copper ion spectroscopically assigned as Cu_C (27), a finding that would be consistentwith either the structural Cu_C or Cu_D site.

In contrast to the Cu_D site, the Cu_C site is only apparent in one map of *M. capsulatus* (Bath) pMMO (table S2 and fig. S15; MC03), with strong density connected to that of the three CuC ligands, Asp^{156} (2.7 Å), His^{160} (2.1 Å), and His^{173} (2.2 Å). The presence of Cu_C correlates with increased disorder in the loop (residues 233 to 240) connecting newly visible helices α3 and α4 in PmoC. Although density for the Cu_D ligands is still observed, there is no density attributable to a metal ion (fig. S15). Similarly, the *M. alcaliphilum* comb. nov. 20Z pMMO map (table S2; 20Z01) exhibits a clear Cu_C site (fig. S17A), but the density for the region corresponding to *M. capsulatus* (Bath) PmoC residues 233 to 240 (residues 206 to 213 in *M. alcaliphilum* comb. nov. 20Z PmoC) is poorly defined (fig. S14A) and completely lacks side-chain density for Arg^{165} (Arg^{137} in *M. alcaliphilum* comb. nov. 20Z PmoC; fig. S17A). There is no obvious density for Cu_D, and nanodisc samples of *M. alcaliphilum* comb. nov. 20Z pMMO exhibit no methane oxidation activity (table S1). The Cu_C site is again observed in the *Methylocystis* sp. str. Rockwell pMMO map, and the region containing the Cu_D ligands (residues 200 to 221), although ordered (fig. S14A), lacks side-chain density

(fig. S17B). Upon further processing of this map using DeepEMhancer (37), the Cu_D site ligands were resolved (fig. S17B). In all six maps, the density at the Cu_C or Cu_D sites is not as strong as that observed at Cu_B, which is consistent with the full Cu_B occupancy observed by crystallography and native top-down mass spectrometry (nTDMS) (14).

In two of the three *M. capsulatus* (Bath) pMMO maps that show density for Cu_D (table S2; MC01 and MC02), there is no density between the Cu_C ligands. By contrast, the crystal structure contains zinc derived from the crystallization buffer at the Cu_C site (Fig. 4C), and crystal structures of pMMO isolated from *Methylocystis* sp. str Rockwell contain copper in this site (10). In the cryo-EM maps lacking density for Cu_C, residue His^{160} adopts a slightly different conformation, presumably because it is no longer stabilized by copper coordination. Instead of Cu_C, a spherical density ~2 Å from the location of Cu_C is observed (Fig. 4B). This density was modeled as a water molecule because it is within hydrogen-bonding—rather than coordinating—distance of Cu_C ligands Asp^{156} and His^{173} as well as Arg^{165} (Fig. 4D). This water molecule is not present in the third map (table S2; MC04). Instead, the density corresponding to Cu_C ligands His^{160} and His^{173} is weakly connected (fig. S18), offering the possibility that the Cu_C and Cu_D sites, separated by ~5.7 Å, might be occupied simultaneously.

Notably, the cryo-EM model of active *M. capsulatus* (Bath) pMMO reveals a hydrophobic cavity adjacent to the Cu_D site (Fig. 4E) extending away from the periplasmic side of pMMO. This cavity is lined by PmoA residues Ile^{39}, Met^{42}, and Leu^{43} and PmoC residues Phe^{177}, Phe^{240}, and Phe^{248}. These three PmoC residues are invariant (Fig. 3D), and the latter two derive from the newly observed region of PmoC. This cavity houses the aforementioned water molecule and abuts the location of the Cu_D ligands (Fig. 4D). Its existence supports assignment of the pMMO active site as one or both of the two copper sites, Cu_C and Cu_D.

All four *M. capsulatus* (Bath) pMMO samples had similar activities and copper contents (Fig. 1A and fig. S3), precluding correlation of the Cu_C and Cu_D occupancies with methane oxidation. Treating the nanodiscs with excess copper after reconstitution did not increase the apparent occupancy of either site and was found to inhibit activity, consistent with previous studies showing the inhibitory effect of excess copper (10). Although we assigned Cu_D as copper on the basis of extensive data linking copper addition to restored activity (10, 14), cryo-EM data, unlike x-ray diffraction data (38), do not allow for unambiguous metal identification. Other possibilities include iron and zinc, but iron does not restore activity to metal-depleted membranes (39), and zinc inhibits activity (10). Additionally, only heme iron, attributed to cytochrome impurities, has been detected spectroscopically in pMMO (40).

To further probe the identity of the metal ion at Cu_D and its role in methane oxidation, metals were removed from *M. capsulatus* (Bath) membranes using potassium cyanide (10, 41), and the sample was split into two batches, one of which was treated with 10 equivalents of $CuSO_4$. pMMO was solubilized from both batches, reconstituted into nanodiscs, and investigated by cryo-EM. A cryo-EM map of the metal-depleted sample, which contained 0.1 equivalents of Cu (fig. S19), was resolved to 3.65 Å (fig. S20A and table S2; MC05). Some density is still observed at Cu_B, but the occupancy of the bis-His site is reduced

substantially (fig. S21A). Whereas the PmoB and PmoA subunits remain intact, the PmoC subunit is completely disrupted (fig. S21A), and the sample exhibits no methane oxidation activity (fig. S22). There is no density for residues 54 to 97, which make up the first helix; residues 160 to 178, including the Cu_C site; and residues 221 to 246, including the Cu_D site. The disordered regions are bracketed by coordinating histidines (Cu_C His^{160} and Cu_D His^{245}), which indicates that PmoC requires copper for structural stability. In addition, all of the stabilized lipids are disrupted in this structure.

The cryo-EM map of the metal-depleted, copper-reloaded sample, which contained ~0.6 equivalents of copper (fig. S19), was resolved to 3.39 Å (fig. S20B and table S2; MC06). Despite the lower resolution, lipids on the inner pore and periphery of pMMO are clearly visible, and the backbone could be traced through the entire PmoC subunit (fig. S21B). Thus, the destabilizing effects of copper removal on structure can be reversed upon copper addition. The Cu_B and bis-His sites are more fully occupied (fig. S21B) as well. Although residues at the Cu_D site are less well defined, there is density near His^{245} and Asn^{227} that could correspond to a metal ion (fig. S21C), supporting the assignment of Cu_D as a copper-binding site. The Cu_C site residues are well defined and oriented toward one another, but the site appears unoccupied (fig. S21C). Notably, this sample also exhibits methane oxidation activity (fig. S22) on par with that observed in pMMO reconstituted into native nanodiscs with no additional copper added (Fig. 1A) and consistent with previous studies showing that ~50% of activity can be regained after cyanide treatment and copper reloading (10). This result links reloading of Cu_D to the recovery of some methane oxidation activity.

These first structures of active pMMO, obtained by embedding the enzyme in a native lipid bilayer, provide critical insight into pMMO structure and function. The combined results indicate that an intact PmoC scaffold, including Cu_C and Cu_D ligands supported by a hydrogen-bonding network and interior lipid bilayer, is associated with enzymatic activity. The presence of Cu_D in most of the *M. capsulatus* (Bath) cryo-EM structures suggests a role in activity, but the occupancy of the Cu_C and Cu_D sites in vivo remains to be determined. The structure of the highly conserved region of PmoC—along with the unexpected discovery of the Cu_D site and adjacent hydrophobic cavity—provide a much more complete picture of the pMMO active site architecture. This substantially revised view of pMMO, obtained after >15 years of crystallographic characterization, underscores the importance of studying membrane proteins in their native environments and the potential of high-resolution cryo-EM combined with membrane mimetic technology.

Supplementary Material

Refer to Web version on PubMed Central for supplementary material.

ACKNOWLEDGMENTS

We thank R. Abdella for advice on data processing, S. Ro for advice on methanotroph handling, J. Pattie for computer support, and J. Remis and R. Purohit for guidance on sample preparation and data collection. Molecular graphics and analyses were performed with UCSF ChimeraX, developed by the Resource for Biocomputing, Visualization, and Informatics at the University of California, San Francisco, with support from National Institutes of Health grant R01-GM129325 and the Office of Cyber Infrastructure and Computational Biology, National Institute of Allergy and Infectious Diseases.

Funding:

This work was supported by National Institutes of Health grants R35GM118035 (A.C.R.), T32GM008382 (C.W.K.), T32GM105538 (F.J.T.), and R01GM135651 (Y.H.). This work used resources of the Northwestern University Structural Biology Facility, which is generously supported by the NCI CCSG P30 CA060553 grant awarded to the Robert H. Lurie Comprehensive Cancer Center. We acknowledge the use of the Ametek K3 direct electron detector, which was generously provided by R. A. Lamb (HHMI investigator). A portion of this research was supported by NIH grant U24GM129547 and performed at the PNCC at OHSU and accessed through EMSL (grid.436923.9), a DOE Office of Science User Facility sponsored by the Office of Biological and Environmental Research. Some of this work was performed at the Stanford-SLAC Cryo-EM Center (S2C2) supported by the NIH Common Fund Transformative High-Resolution Cryoelectron Microscopy program (U24 GM129541). Some of this work was performed at the National Center for CryoEM Access and Training (NCCAT) and the Simons Electron Microscopy Center located at the New York Structural Biology Center, supported by the NIH Common Fund Transformative High-Resolution Cryoelectron Microscopy program (U24GM129539) and by grants from the Simons Foundation (SF349247) and the NY State Assembly.

Data and materials availability:

The models of pMMO from *M. capsulatus* (Bath), pMMO from *M. alcaliphilum* comb. nov. 20Z, and pMMO from *Methylocystis* sp. str. Rockwell have been deposited in the Protein Data Bank with accession codes 7S4H (MC01), 7S4I (MC02), 7S4J (MC03), 7S4K (MC04), 7S4L (20Z01), 7S4M (RW01), 7T4O (MC05), and 7T4P (MC06). The corresponding cryo-EM maps are available at the Electron Microscopy Data Bank (www.ebi.ac.uk/emdb/). All other data are available in the main text or the supplementary materials.

REFERENCES AND NOTES

1. Barrett B, Charles JW, Temte JL, Prev. Med. 70, 69–75 (2015). [PubMed: 25434735]
2. Chai XL, Tonjes DJ, Mahajan D, Prog. Energy Combust. Sci. 56, 33–70 (2016).
3. Curry CL, Global Biogeochem. Cycles 21, GB4012 (2007).
4. Hwang IY et al., Appl. Microbiol. Biotechnol. 102, 3071–3080 (2018). [PubMed: 29492639]
5. Nguyen AD, Lee EY, Trends Biotechnol. 39, 381–396 (2021). [PubMed: 32828555]
6. Koo CW, Rosenzweig AC, Chem. Soc. Rev. 50, 3424–3436 (2021). [PubMed: 33491685]
7. Ross MO, Rosenzweig AC, J. Biol. Inorg. Chem. 22, 307–319 (2017). [PubMed: 27878395]
8. Lieberman RL, Rosenzweig AC, Nature 434, 177–182 (2005). [PubMed: 15674245]
9. Smith SM et al., Biochemistry 50, 10231–10240 (2011). [PubMed: 22013879]
10. Sirajuddin S et al.., J. Biol. Chem. 289, 21782–21794 (2014). [PubMed: 24942740]
11. Ro SY et al., J. Biol. Chem. 293, 10457–10465 (2018). [PubMed: 29739854]
12. Hakemian AS et al., Biochemistry 47, 6793–6801 (2008). [PubMed: 18540635]
13. Koo CW, Rosenzweig AC, “Particulate methane monooxygenase and the PmoD protein” in Encyclopedia of Inorganic and Bioinorganic Chemistry, Scott RA, Ed. (Wiley, 2020).
14. Ro SY et al., Nat. Commun. 10, 2675 (2019). [PubMed: 31209220]
15. Sirajuddin S, Rosenzweig AC, Biochemistry 54, 2283–2294 (2015). [PubMed: 25806595]
16. Garavito RM, Ferguson-Miller S, J. Biol. Chem. 276, 32403–32406 (2001). [PubMed: 11432878]
17. Anishkin A, Loukin SH, Teng J, Kung C, Proc. Natl. Acad. Sci. U.S.A. 111, 7898–7905 (2014). [PubMed: 24850861]
18. Bayburt TH, Sligar SG, FEBS Lett. 584, 1721–1727 (2010). [PubMed: 19836392]
19. Bligh EG, Dyer WJ, Can. J. Biochem. Physiol. 37, 911–917 (1959). [PubMed: 13671378]
20. Folch J, Lees M, Sloane Stanley GH, J. Biol. Chem. 226, 497–509 (1957). [PubMed: 13428781]
21. Cook SA, Shiemke AK, Arch. Biochem. Biophys. 398, 32–40 (2002). [PubMed: 11811946]
22. Peng W, Qu X, Shaik S, Wang B, Nat. Catal. 4, 266–273 (2021).
23. Ross MO et al., Science 364, 566–570 (2019). [PubMed: 31073062]

24. Cutsail GE 3rd, Ross MO, Rosenzweig AC, DeBeer S,Chem. Sci. 12, 6194–6209 (2021). [PubMed: 33996018]
25. Cao L, Caldararu O, Rosenzweig AC, Ryde U, Angew. Chem. Int. Ed. 57, 162–166 (2018).
26. Chang WH et al., J. Am. Chem. Soc. 143, 9922–9932 (2021). [PubMed: 34170126]
27. Jodts RJ et al., J. Am. Chem. Soc. 143, 15358–15368 (2021). [PubMed: 34498465]
28. Lu YJ et al., J. Inorg. Biochem. 196, 110691 (2019). [PubMed: 31063931]
29. Chan SI et al., Angew. Chem. Int. Ed. 46, 1992–1994 (2007).
30. Ng KY, Tu LC, Wang YS, Chan SI, Yu SS,ChemBioChem 9, 1116–1123 (2008). [PubMed: 18383583]
31. Harms MJ, Schlessman JL, Sue GR, García-Moreno E B.,Proc. Natl. Acad. Sci. U.S.A. 108, 18954–18959 (2011). [PubMed: 22080604]
32. Reid CW, Blackburn NT, Clarke AJ, Biochemistry 45, 2129–2138 (2006). [PubMed: 16475802]
33. Vita N. et al., Sci. Rep. 6, 39065 (2016). [PubMed: 27991525]
34. Dennison C, Harrison MD, J. Am. Chem. Soc. 126, 2481–2489 (2004). [PubMed: 14982457]
35. Hart PJ et al., Protein Sci. 5, 2175–2183 (1996). [PubMed: 8931136]
36. Xie Y. et al., J. Biochem. 137, 455–461 (2005). [PubMed: 15858169]
37. Sanchez-Garcia R. et al., Commun. Biol. 4, 874 (2021). [PubMed: 34267316]
38. Bowman SEJ, Bridwell-Rabb J, Drennan CL, Acc. Chem. Res. 49, 695–702 (2016). [PubMed: 26975689]
39. Balasubramanian R. et al., Nature 465, 115–119 (2010). [PubMed: 20410881]
40. Lieberman RL et al., Inorg. Chem. 45, 8372–8381 (2006). [PubMed: 16999437]
41. Smith SM, Balasubramanian R, Rosenzweig AC, Methods Enzymol. 495, 195–210 (2011). [PubMed: 21419923]
42. Tian W, Chen C, Lei X, Zhao J, Liang J, Nucleic Acids Res. 46, W363–W367 (2018). [PubMed: 29860391]

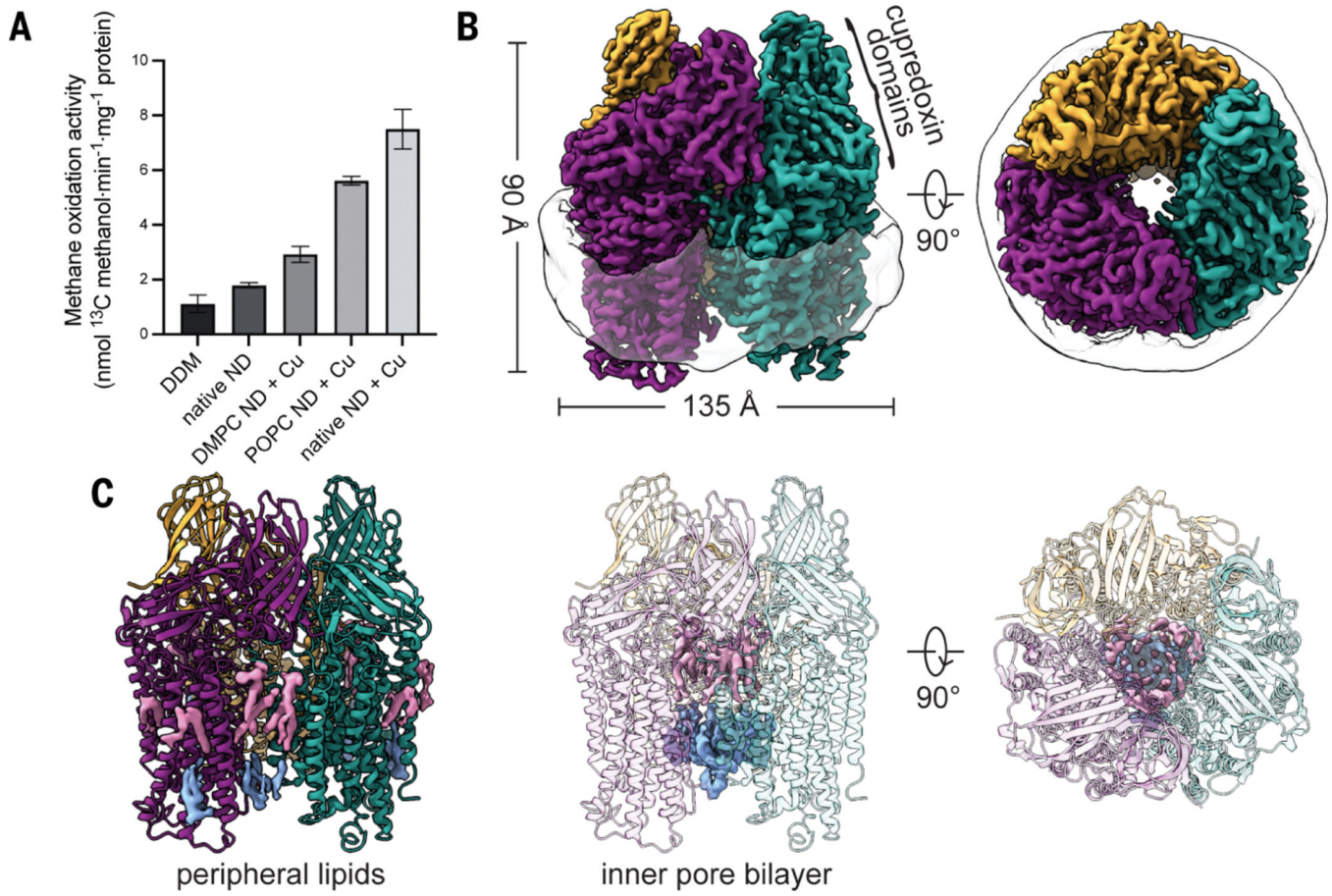

Fig. 1. Structural characterization of *M. capsulatus* (Bath) pMMO in a native lipid nanodisc.

(**A**) Methane oxidation activity of cryo-EM samples. Addition of 3 equivalents of $CuSO_4$ during nanodisc (ND) reconstitution (+ Cu) improved activity. Error bars represent standard deviations of $n \geq 3$ biological replicates, each measured in triplicate. (**B**) Cryo-EM map (dataset MC01) showing the trimer and the encircling nanodisc. Symmetrical αβγ protomers are colored in purple, teal, and gold, respectively.(**C**) Model of pMMO showing the map for lipids on the periphery and in the inner pore of the enzyme. The periplasmic and cytoplasmic leaflets are colored in pink and blue, respectively.

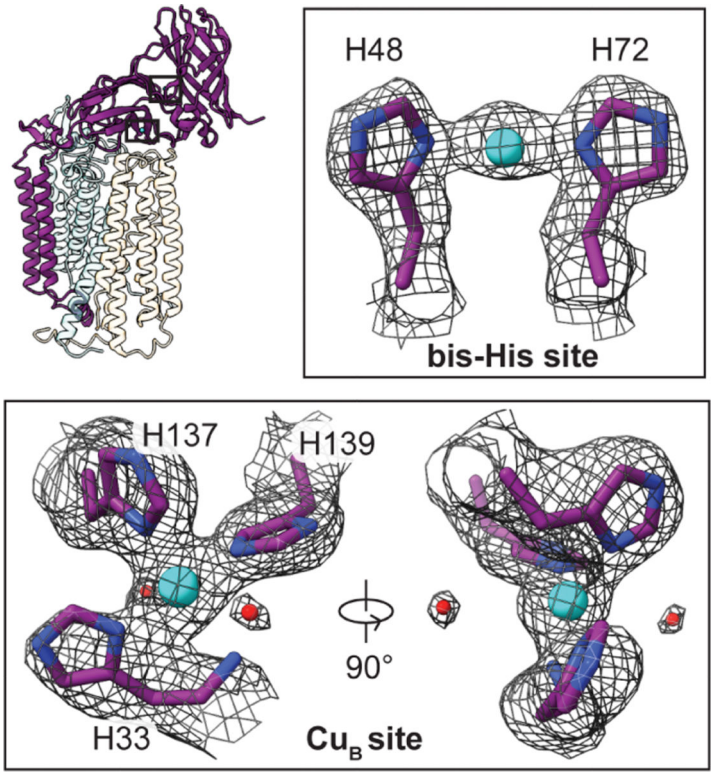

Fig. 2. Copper sites in the PmoB subunit of *M. capsulatus* (Bath) pMMO.

The protomer model is shown with the PmoB subunit highlighted and the regions housing the copper sites boxed. Copper ions and water molecules are shown as cyan and red spheres, respectively. The cryo-EM map (MC01) is shown as a gray mesh.

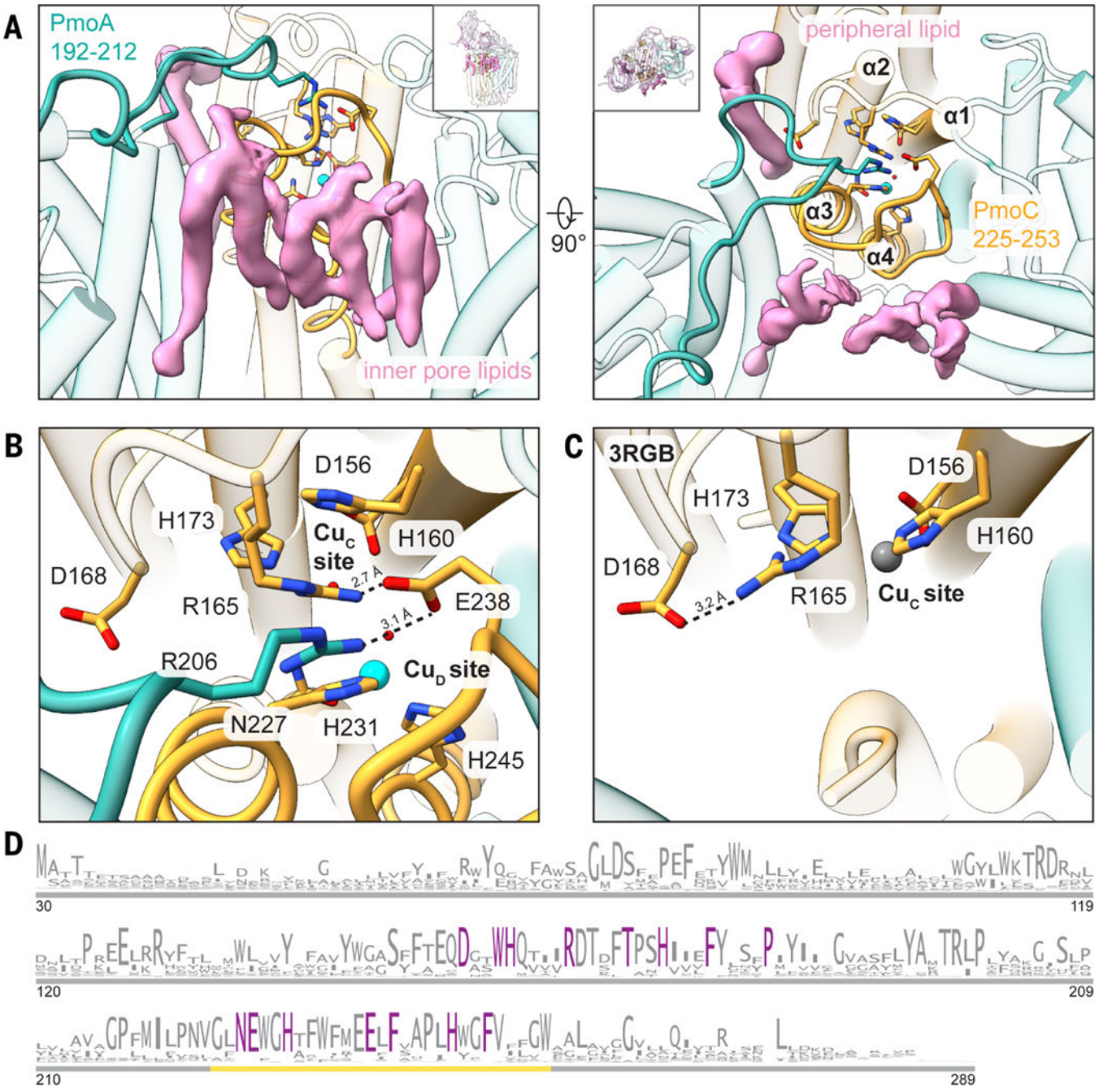

Fig. 3. Regions of *M. capsulatus* (Bath) pMMO newly observed in the cryo-EM structures.

(**A**) Newly modeled residues in PmoA (192 to 212) (left) and PmoC (225 to 253) (right) are highlighted in teal and gold, respectively. Cryo-EM densities corresponding to lipids that interact with these regions are shown in pink. (**B**) Magnified view of the completed four-helix bundle from the cryo-EM structure (MC01). Key residues are labeled, and the hydrogen-bonding network involving Arg^{206} (PmoA), Glu^{238} (PmoC), and Arg^{165} (PmoC) is marked with dashed lines. The CuD site copper ion is shown as a cyan sphere. (**C**) Magnified view of the same region shown in (B) in the crystal structure (Protein Data Bank ID: 3RGB) (9), with the hydrogen bond between Asp^{168} and Arg^{165} shown as a dashed line.

The zinc ion occupying the Cu_C site is shown as a gray sphere. (**D**) Sequence logo for the PmoC subunit (PF04896). Only sequences found in pMMO or ammonia monooxygenase operons are included. Residues conserved at 100% are colored in purple. The gold line demarcates the newly stabilized region in the cryo-EM structures. Single-letter abbreviations for the amino acid residues are as follows: A, Ala; C, Cys; D, Asp; E, Glu; F, Phe; G, Gly; H, His; I, Ile; K, Lys; L, Leu; M, Met; N, Asn; P, Pro; Q, Gln; R, Arg; S, Ser; T, Thr; V, Val; W, Trp; and Y, Tyr.

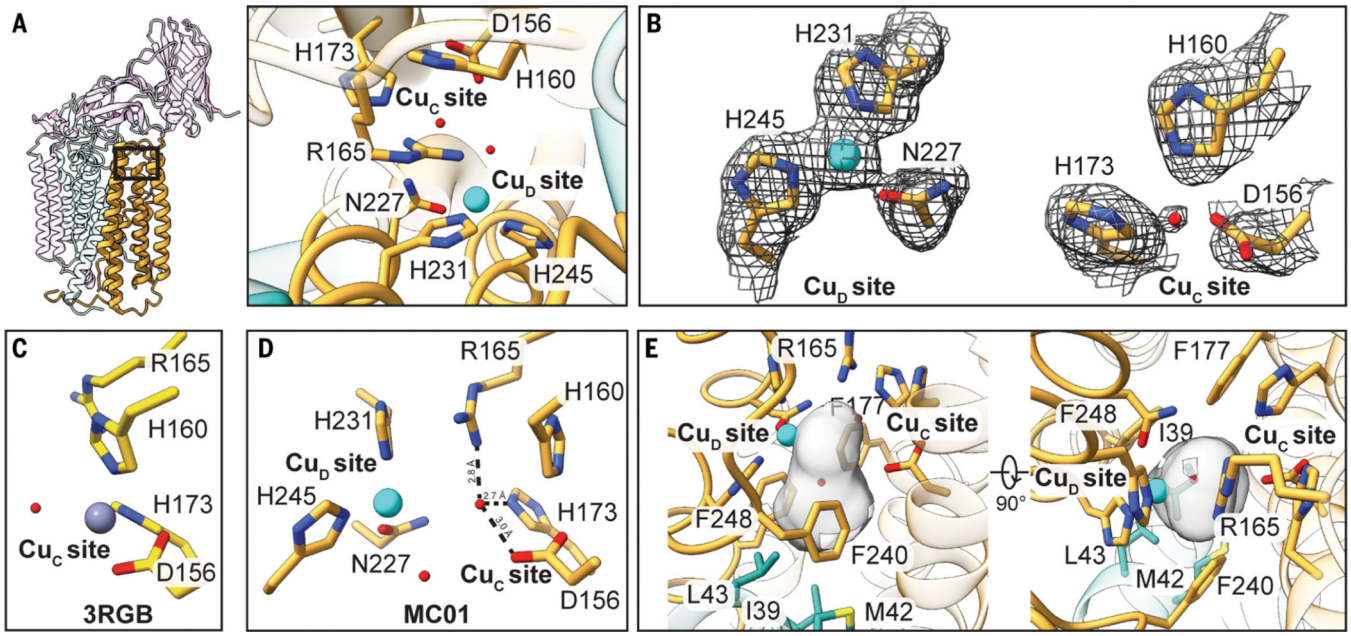

Fig. 4. Active site architecture in the PmoC subunit of *M. capsulatus* (Bath) pMMO.

(**A**) The protomer is shown with the PmoC subunit highlighted and the region housing the metal-binding sites boxed (left) and as a magnified top-down view (right). (**B**) The map (MC01) at the Cu_D and Cu_C sites. (**C**) The corresponding model for the crystal structure (Protein Data Bank ID: 3RGB) (9) in which the Cu_C site is occupied by zinc. The model lacks residues 225 to 253, which include the Cu_D site residues. (**D**) Overall model of Cu_C and Cu_D sites, with hydrogen bonds involving the water molecule in the Cu_C site shown as dashed lines. (**E**) Cavity located between and below the two sites shown in gray, generated using CASTp (42). Residues lining the cavity are labeled.